Aluminium substituted yttrium iron garnet thin films with reduced Curie temperature

D. Scheffler [1], O. Steuer,[2,3] S. Zhou,[3] L. Siegl,[4] S. T. B. Goennenwein,[4] and M. Lammel [4]

[1]*Institute of Solid State and Materials Physics, Technische Universitaet Dresden, 01062 Dresden, Germany*
[2]*Institute of Materials Science, Technische Universitaet Dresden, 01069 Dresden, Germany*
[3]*Institute of Ion Beam Physics and Materials Research, Helmholtz Zentrum Dresden-Rossendorf, 01328 Dresden, Germany*
[4]*Department of Physics, University of Konstanz, 78457 Konstanz, Germany*

Magnetic garnets such as yttrium iron garnet ($Y_3Fe_5O_{12}$, YIG) are widely used in spintronic and magnonic devices. Their magnetic and magneto-optical properties can be modified over a wide range by tailoring their chemical composition. Here, we report the successful growth of Al-substituted yttrium iron garnet (YAlIG) thin films via radio frequency sputtering in combination with an *ex situ* annealing step. Upon selecting appropriate process parameters, we obtain highly crystalline YAlIG films with different Al^{3+} substitution levels on both single crystalline $Y_3Al_5O_{12}$ (YAG) and $Gd_3Ga_5O_{12}$ (GGG) substrates. With increasing Al^{3+} substitution levels, we observe a reduction of the saturation magnetization as well as a systematic decrease of the magnetic ordering temperature to values well below room temperature. YAlIG thin films thus provide an interesting material platform for spintronic and magnonic experiments in different magnetic phases.

I. INTRODUCTION

In the field of insulator spintronics, magnetic materials are usually used in their ordered phase, i.e. well below their respective magnetic ordering temperature [1–9]. Therefore, also almost all spin transport experiments have been performed in the ferro, ferri or antiferromagnetic phase [1–9]. Moreover, a few attempts to study spin transport in the paramagnetic phase have also been made, either by using paramagnetic materials [10–12], or by performing the experiments at elevated temperatures above the ordering temperature [13–15]. A comprehensive understanding of spin transport in the paramagnetic phase nevertheless is lacking, not to mention its evolution across the magnetic phase transition. This makes systematic experiments across the magnetic phase transition, i.e., from the ferromagnetic to the paramagnetic phase, highly desirable to establish a robust understanding of spin transfer as well as magnon generation and propagation processes. In addition, magnetic fluctuations are enhanced around the phase transition, allowing to study the impact of such fluctuations on spin transport.

The prototype material for spin transport studies [2–7,13,16] is the magnetic insulator yttrium iron garnet $Y_3Fe_5O_{12}$ (YIG), as it has a very low Gilbert damping parameter [17–20] and a small coercive field [17,20,21]. This makes YIG an ideal material for magnon transport experiments and spin Hall effect driven spin transport studies [2–7,13,16]. However, YIG has proven problematic for spin transport experiments across the magnetic phase transition

due to its relatively high Curie temperature of $T_c = 559$ K [22]. Experiments at temperatures close to or above T_c are hampered by a finite thermally induced electrical conductivity of YIG [23]. In addition, a significant interdiffusion of Pt in YIG/Pt heterostructures has been reported for $T > 470$ K, which leads to a significant deterioration of the interface and the magnetic properties of YIG [13].

One way to circumvent such high temperature issues is to lower T_c. As the magnetic properties of YIG are defined by the Fe^{3+} ions, a lower T_c can be achieved by substituting the Fe^{3+} ions with nonmagnetic ions. This has been successfully accomplished almost exclusively for bulk crystals by substituting with, amongst others, Al^{3+} ions [24–31]. By increasing the Al^{3+} substitution, both Curie temperature T_c and saturation magnetization M_s are reduced. Sufficiently high substitution levels x allow to tailor T_c of the resulting yttrium aluminium iron garnet ($Y_3Al_xFe_{5-x}O_{12}$, YAlIG) from the value of pure YIG down to values well below room temperature. It has been shown that the desired magnetic properties of YIG such as low magnetic damping and low coercivity are conserved upon substitution with Al^{3+} ions [24,32]. However, the studies of YAlIG are almost exclusively limited to bulk and powder materials [24–31], while thin films are required for typical spintronic devices. So far, only YAlIG thin films up to $x = 0.783$ were investigated [33], which is not sufficient to reduce T_c down to room temperature.

Here, we report the successful fabrication of YAlIG thin films with different Al^{3+} substitution levels $1.5 \leqslant x \leqslant 2$ by radio-frequency (RF) sputtering deposition and a subsequent annealing step. We evaluate the influence of the Al^{3+} substitution level on the structural and magnetic properties of our thin films. To this end, we study the impact of different substrate materials and annealing temperatures on the structural and magnetic quality. X-ray diffraction (XRD) is utilized to show that our sputtered and post-annealed YAlIG

TABLE I. Summary of nominal Al^{3+} substitution level x, annealing temperature T_A, thickness t, lattice parameters a (length) and α (angle), saturation magnetization M_s at 20 K, Curie temperature T_c, and the upper limit for the Curie temperature $T_{c,max}$ for the $Y_3Al_xFe_{5-x}O_{12}$ films.

Substrate	x	T_A (°C)	t (nm)	a_{YAlIG} (nm)	α (deg)	M_s @ 20 K (kAm^{-1})	T_c (K)	$T_{c,max}$ (K)
YAG	1.5	as-dep.	50	Amorphous	Amorphous	<5	–	–
YAG	1.5	700	45	1.2276	90	41	270	300
YAG	1.5	800	45	1.2276	90	41	262	300
YAG	1.75	800	37	1.2266	90	16	156	190
YAG	2	800	45	1.2205	90	10	102	140
GGG	1.5	as-dep.	50	Amorphous	Amorphous			
GGG	1.5	700	45	1.2355	90.46			
GGG	1.5	800	45	1.2348	90.49			

thin films have a high crystal quality. SQUID vibrating sample magnetometry demonstrates the successful reduction of T_c to values well below room temperature, as well as coercive fields comparable to pure YIG films. We utilize broadband ferromagnetic resonance measurements to investigate the dynamic magnetic properties and the magnetic anisotropy of our YAlIG thin films.

II. EXPERIMENTAL METHODS

The YAlIG films were grown on commercially available (111)-oriented single crystalline yttrium aluminium garnet ($Y_3Al_5O_{12}$, YAG, cubic lattice parameter $a_{YAG} = 1.201$ nm) and gadolinium gallium garnet ($Gd_3Ga_5O_{12}$, GGG, $a_{GGG} = 1.240$ nm) substrates by RF sputtering in a UHV system (base pressure below 1×10^{-8} mbar). Three different two inch diameter targets with Al^{3+} substitution levels of $x = 1.5, 1.75,$ and 2 were used. These substitution levels were selected to obtain thin films with a Curie temperature T_c close to or below room temperature based on the existing literature for bulk YAlIG [25,28,31].

Prior to deposition, the substrates were cleaned subsequently in acetone, isopropanol, and distilled water in a ultrasonic bath for 10 min each. After transferring the substrates into the sputtering chamber, they were annealed *in situ* at 200 °C for 1 h in a vacuum to eliminate residual adsorbed water. The YAlIG films were deposited at room temperature. The thermal energy for the crystallization of the YAlIG thin films was provided by an *ex situ* postannealing in a two-zone furnace. Temperatures of 700 °C and above were reported to be sufficient for a complete crystallization of YIG thin films of comparable thickness [34–36]. The partial oxygen pressure was applied to counteract oxygen losses of the films during the annealing [35]. All samples examined in this study are summarized in Table I. The detailed deposition and annealing parameters are summarized in Table II.

Various x-ray diffraction measurements (symmetrical $2\theta - \omega$ scan, ω scan, reciprocal space mapping) were performed using Cu-$K_{\alpha 1}$ radiation ($\lambda = 0.15406$ nm) to evaluate the structural properties of the film. X-ray reflectivity was used to measure the film thickness.

Rutherford backscattering spectroscopy random (RBS/R) experiments at a backscattering angle of 170° were performed to investigate the chemical composition of selected YAlIG films, using a 1.7 keV He$^+$ ion beam with a diameter of about 1 mm, generated by a 2 MV van-de-Graaff accelerator. The

backscattering angle was 170°. The measured data was fitted to a calculated spectra using the *SIMNRA* software [37]. Due to the low mass of oxygen, only the elemental ratios between Fe, Al, and Y are used for quantitative analysis of the chemical composition.

The static magnetic properties were investigated by superconducting quantum interference device vibrating sample magnetometry (SQUID VSM). For an external magnetic field orientation within the sample plane during the measurement (in-plane, ip), the sample was mounted onto a quartz rod; for an orientation of the external magnetic field parallel to the surface normal (out-of-plane, oop) the sample was mounted between plastic straws. The magnetic moment of the sample was recorded in dependence of the external field (maximum field $\mu_0 H_{max} = \pm 3$ T, minimal field steps of $\Delta \mu_0 H = 2$ mT) and the temperature (2 K to 360 K, temperature steps $\Delta T = 2$ K). Note that due to the large paramagnetic background signal of the GGG substrate and the correspondingly larger background subtraction error, we focused on the YAlIG thin films on YAG substrates for the magnetization characterization. For all magnetometry data shown in this work, the magnetic contributions of the YAG substrate were subtracted. For temperature dependent measurements, this includes the diamagnetic contribution and an additional paramagnetic contribution from contaminations within the YAG substrate, which combined where fitted to $m_{sub} = a/(T + b) + c$ with a, b, and c as fitting parameters. For field dependent measurements, the substrate contribution is defined by the linear slope at high fields.

Broadband ferromagnetic resonance (bb-FMR) measurements were performed to investigate the dynamic magnetic

TABLE II. Summary of the deposition and annealing parameters for the fabrication of the YAlIG thin films.

Sputter deposition	Target-substrate distance	206 mm
	Sample holder rotation rate	5 rpm
	Pressure (Ar)	4.3×10^{-3} mbar
	Ar flow rate	20 sccm
	Sputtering power	75 W
Annealing	Heating rate	15 K/min
	Pressure (O$_2$)	3 mbar
	Annealing temperature	700 − 800 °C
	Annealing time	240 min

properties and the magnetic anisotropy of two representative samples, both with similar nominal composition and annealing temperature($x = 1.5$, $T_A = 800$ °C), but on different substrates. Therefore, the samples are placed on a coplanar wave guide (CPW) with the thin film facing toward the center conductor of the CPW. The CPW is connected to two ports of a vector network analyzer (VNA, PNA N5225B from Keysight). To control the temperature of the sample and to apply an external magnetic field, the CPW assembly was inserted into a 3D vector magnet cryostat. Using the VNA, we record the complex microwave transmission parameter S_{21} as a function of frequency $f = 1 - 30$ GHz at several fixed static magnetic fields H. The magnetic field was applied either parallel (ip) or perpendicular (oop) to the sample plane. The measured S_{21} was corrected for the frequency dependent and magnetic field dependent background (see moving field reference method in [38]) and fitted by a complex Lorentzian function to extract the FMR resonance frequency f_{res} and linewidth Δf.

III. RESULTS

A. Structural characterisation

X-ray diffraction measurements carried out on YAlIG thin films with different compositions revealed a high crystalline quality of the respective YAlIG thin films after the annealing step. The symmetrical $2\theta-\omega$ XRD scans of YAlIG thin films with different substitution levels grown on YAG are shown in Fig. 1(a). No diffraction peak that can be ascribed to the YAlIG thin films is observed prior to annealing, supporting the notion that the thermal energy during deposition is not sufficient for crystallization. The necessary thermal energy is provided by the subsequent annealing step, which leads to the crystallization of the YAlIG layer. For all chemical compositions the crystalline nature of the annealed thin films is validated by the diffraction peak which corresponds to YAlIG (444) planes. For substituted yttrium iron garnet, the lattice parameter is changing according to the size of the substitute ion [39]. As Al^{3+} is smaller than Fe^{3+}, the lattice parameters of the YAlIG thin films (cp. Table I) are reduced compared to YIG ($a_{\text{YIG}} = 1.2376$ nm [39]), as expected. Likewise, the lattice parameter is decreasing toward higher substitution levels, which becomes apparent by the shift toward higher diffraction angles. The lattice parameter falls well within the range given by the literature (1.2235 nm $\leqslant$ $a_{\text{YAlIG}} \leqslant 1.2276$ nm) [25,30,39–42], which is illustrated by the gray dashed lines in Fig. 1(a) for $x = 1.5$. Comparing the XRD patterns does not indicate any influence of the annealing temperature on the maximum peak position of thin films with the same Al^{3+} substitution level, aside from a small change in the peak intensity. This might indicate a more complete crystallization at higher temperatures.

A slight peak asymmetry toward lower diffraction angles can be observed independently from the annealing condition or chemical composition which might originate from a partially strained film or a gradient of chemical composition due to diffusion of Al^{3+} from the substrate into the film. Since the lattice mismatch ϵ between the YAG substrate and our YAlIG thin film is relatively high ($\epsilon = \frac{a_{\text{YAlIG}} - a_{\text{sub}}}{a_{sub}} = 2.23\%$, 2.14%, and1.63% for $x = 1.5$, 1.75, and 2) [43], we anticipate
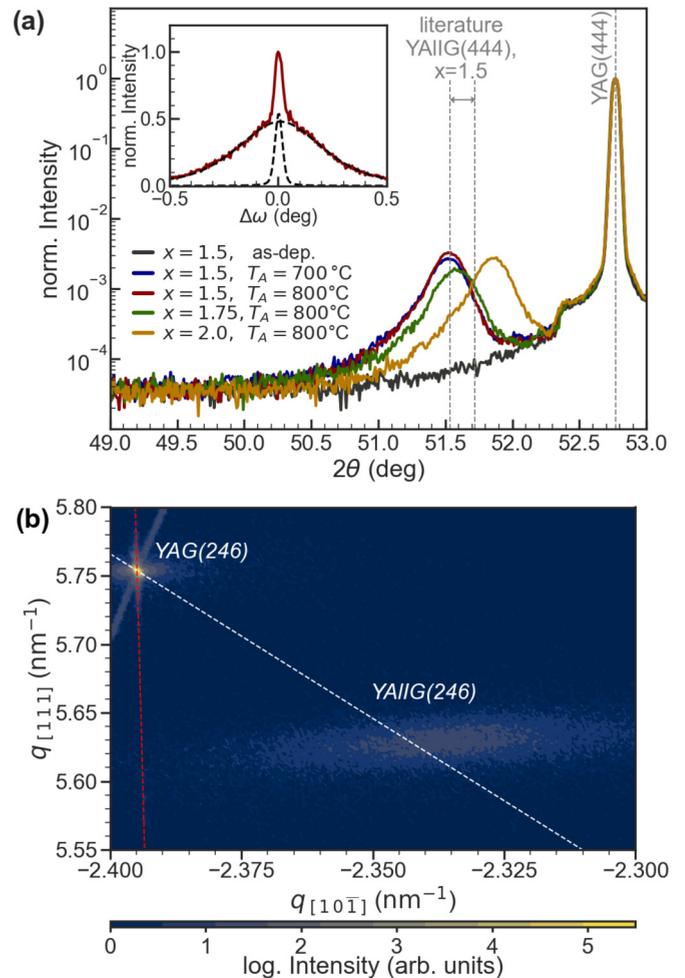

FIG. 1. XRD-analysis of YAG/YAlIG films: (a) Symmetric $2\theta-\omega$ scan for different annealing conditions and compositions. The two gray dashed lines denote the range of values reported in literature for $x = 1.5$ [25,30,39–42]. The inset shows the ω scan of the YAlIG film annealed at 800 °C, $x = 1.5$. The dashed lines indicate the numerical fit of the data to two independent Pseudo-Voigt functions. (b) RSM of the asymmetric (246)-peak of a sample annealed at 800 °C, $x = 1.5$. The white dashed line indicates the peak position for a growth of fully relaxed YAlIG and the red dashed lines indicates the peak position for a growth of fully strained YAlIG.

a relaxed growth for the given film thickness. This is confirmed by reciprocal space mapping [RSM, cp. Fig. 1(b)], as the asymmetric YAlIG (246) peak is located on the calculated line for a fully relaxed crystal. Although the lattice mismatch is reduced at higher substitution levels, no change of the described growth mechanism is found. Further structural investigations via RSM to explain the peak asymmetry observed in the $2\theta-\omega$ XRD scan are not possible due to the low intensity of the asymmetric (246) peak. The ω scan of a YAlIG film annealed at $T_A = 800$ °C, given in the inset of Fig. 1(a), shows a superposition of two diffraction peaks with different full width at half maximum (FWHM) values centered around the same diffraction angle. The FWHM of each peak was determined by numerically fitting the data to the sum of two Pseudo-Voigt functions as 0.04° and 0.46°. A similar behavior has been reported for different heteroepitaxially relaxed thin
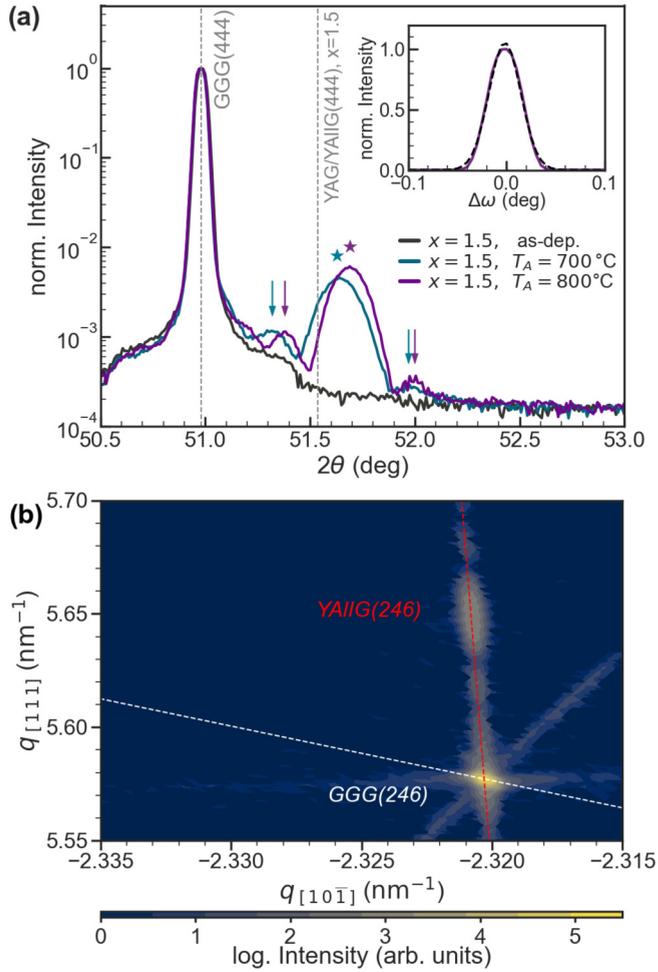
FIG. 2. XRD-analysis of GGG/YAlIG films with $x = 1.5$: (a) Symmetric $2\theta - \omega$ scan of films annealed at different temperatures. The ⋆ indicates the YAlIG (444) peak, the arrows indicate the first Laue oscillation of YAlIG. The inset shows the ω scan of the YAlIG film annealed at $800\,°C$. The dashed line indicates the numerical fit of the data to a Pseudo-Voigt function. (b) RSM of the asymmetric (246) peak of a sample annealed at $800\,°C$, where the white dashed line indicates the peak position for a growth of fully relaxed YAlIG and the red dashed lines indicate the peak position for a growth of fully strained YAlIG.

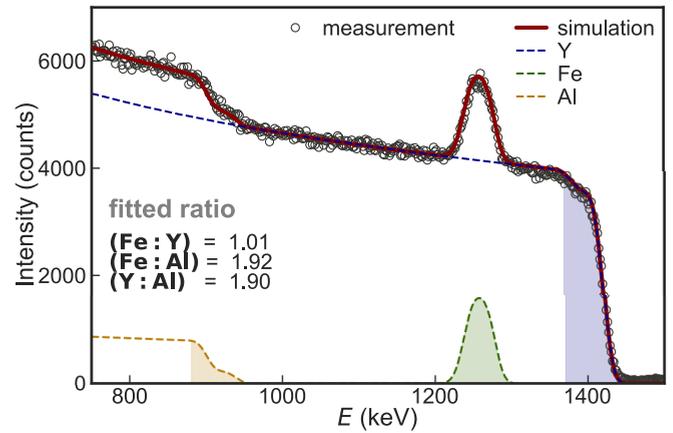FIG. 3. RBS spectra for a YAlIG film with $x = 1.5$ on YAG annealed at $T_A = 800\,°C$. The shaded areas indicate the thin film contribution of the RBS spectra.

film materials [44–48]. The sharp peak is associated with areas of higher structural order, i.e., an epitaxially strained crystalline layer close to the substrate/film interface. Upon further crystallization, the influence of the substrate decreases and the film continues to grow relaxed with the incorporation of defects like dislocations or a higher mosaicity, which is ascribed to the broad peak feature. As 91% of the total peak area contributes to the broad peak, we conclude that the majority of the film features a higher degree of defects.

To evaluate the effect of a smaller lattice mismatch, YAlIG samples with $x = 1.5$ were also prepared on GGG substrates. This reduces the lattice mismatch down to -1%. As for the samples grown on YAG, a post-annealing step is necessary for the crystallization of YAlIG (444) [cp. Fig. 2(a)]. However, the peak position of YAlIG (444) in the symmetrical $2\theta - \omega$ XRD scan is shifted toward higher diffraction angles

compared to the YAlIG samples grown on YAG, visualized by the gray dashed line. This reduction of the distance between the YAlIG (111) lattice planes indicates a fully strained growth of YAlIG on GGG due to the reduced lattice mismatch while keeping the film thickness at 45 nm. This is confirmed by RSM analysis [cp. Fig. 2(b)], as the asymmetric YAlIG (246) diffraction peak is located on the calculated line for a fully strained film. Hence, YAlIG is strained in the film plane and compressed perpendicular to the film surface in comparison to cubic YAlIG, resulting in a rhomboidal YAlIG crystal. The lattice parameters based on the RSM are summaried in Table I. The high crystalline quality of the YAlIG thin films on GGG is confirmed by the very low FWHM of $0.04°$ in the ω scan [cp. Fig. 2(a), inset], which is in the range of the resolution of the x-ray measuring device. In addition, the first Laue oscillation is visible in the symmetric $2\theta - \omega$ scan, indicating high structural ordering of the film. The increase in lattice parameter α, the angle between the unit cell vectors, suggests an enhancement of the strain for higher annealing temperatures. We attribute this to a change of lattice mismatch at higher temperatures due to different thermal coefficients of substrate and film, which was shown for different rare earth garnets [49].

B. Chemical composition

RBS measurements were performed for selected samples to investigate the chemical composition, revealing a significant deviation of the nominal composition. Here, we will present and discuss the RBS results exemplary for a YAlIG film ($x = 1.5$, $T_A = 800\,°C$) on YAG as given in Fig. 3, however, similar correlations were found for all investigated samples.

Going from high backscattered ion energy to lower energies of the spectrum, the elemental contributions of Y, Fe, Al, and O (not shown in Fig. 3) can be distinguished. The first approximately 80 keV of each elemental contribution belong to the YAlIG thin film, indicated by the colored areas in Fig. 3. As both the film and the YAG substrate contain Y, Al, and O, the respective contributions of the film are superimposed by high mass contributions originating from

the substrate toward lower energies. The simulated spectrum (cp. solid line in Fig. 3) is in good agreement to the measurement and the elemental ratios are determined from the fit as (Fe : Y) = 1.01, (Fe : Al) = 1.92, and (Y : Al) = 1.90. These values differ from the values for the nominal stoichiometric composition of the target for $x = 1.5$, i.e., (Fe : Y)$_{target}$ = 1.17, (Fe : Al)$_{target}$ = 2.33, and (Y : Al)$_{target}$ = 2. The most significant change is the decreased (Fe : Al) ratio, indicating a lowered Fe content and an increased Al content. This is confirmed by the decrease of the (Fe : Y) ratio and the (Y : Al) ratio. Therefore, we conclude that our YAlIG films have a lower Fe^{3+} content and an increased Al^{3+} content compared to the chemical composition of the target, while there's no significant change of the Y^{3+} content. We attribute this difference to changes of the chemical composition during the sputtering process, where it was shown that the chemical composition can be altered by different process conditions [50,51]. This has the potential to enable finetuning of the chemical composition by adjusting the deposition process.

C. Magnetometry

The SQUID VSM measurements demonstrate ferromagnetism with a reduced Curie temperature that scales with the Al^{3+} substitution level for YAlIG thin films grown on YAG substrates. The temperature dependent magnetization is given in Fig. 4(a). For the as-deposited sample, no net magnetization was observed in the M(T) curve. Upon annealing and crystallizing into YAlIG, a magnetic phase transition emerges. The Curie temperature for all substitution levels is substantially lowered with respect to that of pure YIG ($T_c = 599$ K) [22], as expected by theory and previous studies in YAlIG [25,27,30], since the ferrimagnetic coupling between the Fe^{3+} ion sublattices is weakened by the substitution of Fe^{3+} ions with nonmagnetic Al^{3+} ions. Consequentially, T_c decreases for higher substitution levels which is also represented in our data. Experimentally, the ferrimagnetic-paramagnetic transition at T_c is broadened by the presence of the static magnetic field of $\mu_0 H = 0.1$ T, by nonuniform temperature sweep rates, and by inhomogeneities of composition within the sample. Therefore, T_c was determined at the minimum of the first derivative of the magnetization with respect to the temperature $\frac{dM}{dT}$ [cp. Fig. 4(b)]. In addition, we define the upper limit for the Curie temperature $T_{c,max}$ at the first temperature where $\frac{dM}{dT}$ is below the noise level of the measurement. Both T_c and $T_{c,max}$ for all YAG/YAlIG samples are summarized in Table I.

Regarding the nominal ratio (Fe : Al)$_{target}$, the measured T_c of our YAlIG thin films is significantly lower than that reported in the literature [25–29,31], as displayed in Fig. 5. However, taking into account the actual (Fe : Al) ratio of the YAlIG thin film, as measured by RBS, and the maximum Curie temperature $T_{c,max}$, the measured T_c of our YAlIG thin films is consistent with the literature, as indicated by the arrows and errorbars in Fig 5. In addition to the chemical composition, other effects might cause a reduction of the Curie temperature. For bulk YAlIG, the distribution of Fe^{3+}/Al^{3+} among the a site and d site within the garnet structure could be altered by different annealing conditions, which leads to a change of Curie temperature and saturation magnetization [27]. While the latter is strongly influenced by the changed
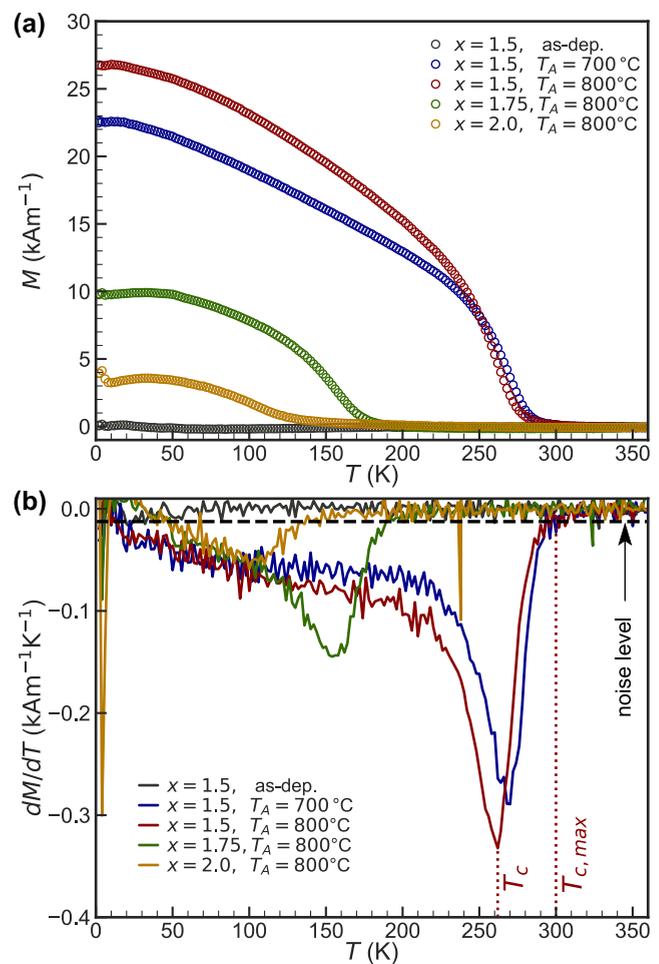

FIG. 4. (a) SQUID-VSM $M(T)$ measurements with a static field of $\mu_0 H = 0.1$ T applied in the film plane. The Curie temperature T_c was determined at the minimum of the first derivative $\frac{dM}{dT}$ (b). To get an upper limit of the Curie temperature, $T_{c,max}$ was determined at the temperature were the first derivative is lower as the noise level, which is indicated as a dashed black line.

distribution, only small changes for the Curie temperature of below 10 K are reported. Since our rare earth garnet thin films feature thicknesses $t \geqslant 37$ nm, dimensionality effects on the Curie temperature should not be relevant [52,53].

The magnetization in dependence of the externally applied magnetic field at 20 K for different Al^{3+} substitution levels x is given in Fig. 6(a). The observed hysteresis loop further corroborates the ferrimagnetic ordering of the YAlIG film at low temperatures. Above 1 T the YAlIG thin films are saturated. The saturation magnetization M_s for each sample is summarized in Table I. As already implied by the M(T) curves, the field dependent measurements show a decreasing M_s toward higher substitution levels. This is explained by the predominant substitution of Fe^{3+} on the tetrahedral sites in YAlIG [25]. Please note that the amorphous, as-deposited sample shows a hysteresis with $M_s = 5$ kAm^{-1}, although no sign of ferrimagnetism was observed in the temperature dependent measurements [cp. Fig. 4(a)]. We attribute this apparent absence of ferrimagnetic order in the M(T) measurements to the subtraction of the paramagnetic background,
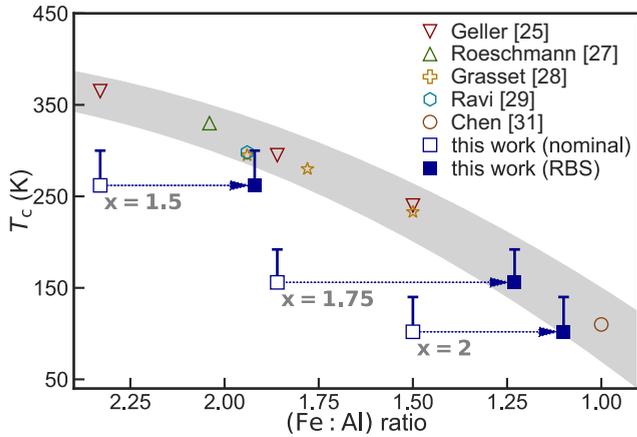
FIG. 5. Curie temperature T_c of YAlIG with different Fe:Al ratios, reported in the literature [25,27–29,31,39] and the results of this study. The shaded area is a guide for the eye for the expected range of T_c based on the literature. For the results of this study, the errorbars indicate the upper limit $T_{c,max}$ and the arrow indicates the shift due to the difference between the nominal $(Fe : Al)_{target}$ ratio and the $(Fe : Al)$ ratio measured via RBS.

which is particularly delicate for samples with an inherently small ferrimagnetic magnetization. The ferrimagnetism of the as-deposited sample can be explained by iron rich areas within the film which can couple ferrimagnetically. However, as the as-deposited YAlIG thin films exhibit no signs of a crystalline ordering, the ferrimagnetism is expected to be weak compared to the annealed and crystallized YAlIG samples, which is corroborated by the temperature as well as the field dependence of the magnetization (cp. Figs. 4 and 6).

To extract the coercivity of the YAlIG thin films, the magnetic hysteresis curves at different temperatures and sample orientations at low fields $\mu_0 H < 100$ mT are representatively shown in Fig. 6(b) for a YAlIG thin film with $x = 1.5$. At 300 K, almost no coercivity and magnetization can be measured as the sample is in vicinity of the Curie temperature ($T_c = 262$ K, $T_{c,max} = 300$ K). As reported for rare earth garnet thin films, the coercive field of our YAlIG thin films increases with lower temperatures [54,55]. For an external magnetic field applied in the sample plane, the coercive field of $\mu_0 H_c = 15$ mT at 20 K and $\mu_0 H_c = 1$ mT at 100 K are in the order of the coercive fields of yttrium iron garnet thin films grown by magnetron sputtering on YAG [55]. No square loop is observed for either field direction in our YAlIG thin films. The x-ray analysis suggests the existence of crystal defects, which might act as pinning centers for the domain wall motion. However, the absence of a distinct magnetic hard axis cannot solely be ascribed to a pinning of the domain walls at defects within the film during the reversal of the magnetization. Therefore, we suspect that our YAlIG thin films exhibit an additional magnetic anisotropy perpendicular to the film surface compensating the shape anisotropy.

D. Ferromagnetic resonance

The bb-FMR measurements demonstrate that the substrate-dependent epitaxial deformation can induce perpendicular magnetic anisotropy in the YAlIG thin films. The dynamic
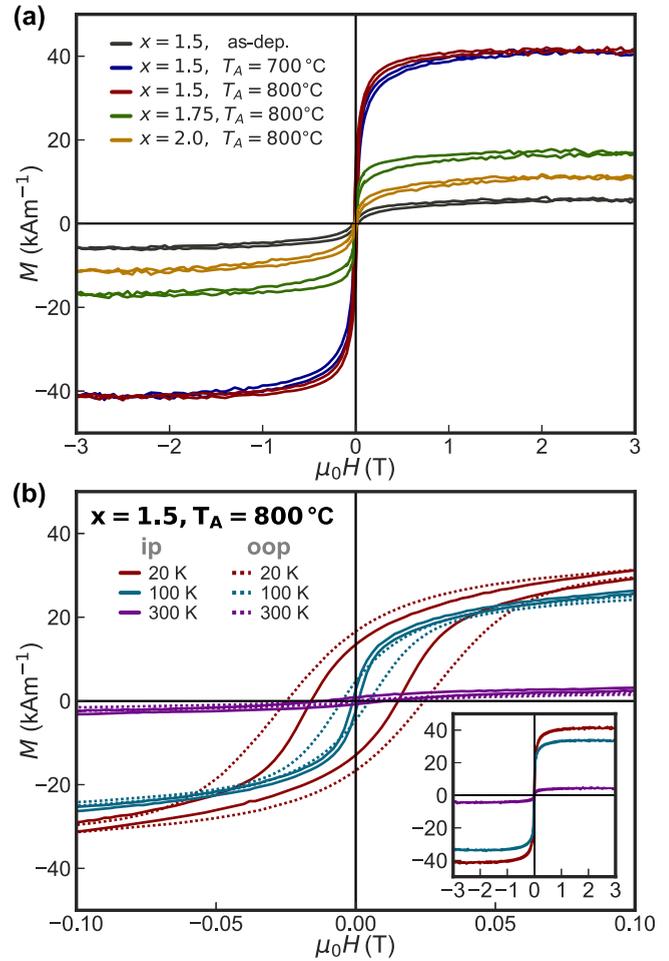

FIG. 6. SQUID-VSM $M(H)$ hysteresis loops of YAlIG thin films grown on YAG. (a) In-plane $M(H)$ hysteresis loops up to $\mu_0 H = \pm 3$ T at 20 K for different annealing temperatures and compositions. (b) In-plane $M(H)$ hysteresis loops at different temperatures for fields up to $\mu_0 H = \pm 0.1$ T for a sample with $x = 1.5$ annealed at $T_A = 800$ °C. The inset shows the complete field range of $\mu_0 H = \pm 3$ T.

magnetic properties of our YAlIG thin films are comparable to those of other rare earth garnet thin films. Two representative samples with the same nominal chemical composition of $x = 1.5$, which were both annealed at $T_A = 800$ °C for 4 h, but on different substrates, have been used. The FMR resonance frequencies f_{res} as a function of magnetic field H at 200 K for the YAlIG thin film on YAG and GGG are shown in Figs. 7(a) and 7(b), respectively. The measurement temperature of 200 K has been chosen to be below the Curie temperature of YAlIG on YAG measured by SQUID VSM ($T_c = 262$ K). The existence of the FMR signal confirms the ferrimagnetic nature of the YAlIG thin film.

To extract the g factor, g, and the effective magnetization M_{eff}, we model f_{res} using the approach of Baselgia *et al.* [56] based on the total free energy density F given by

$$F = -\mu_0 M_s H(sin\theta_M sin\theta_H cos(\phi_M - \phi_H) + cos\theta_M cos\theta_H)$$
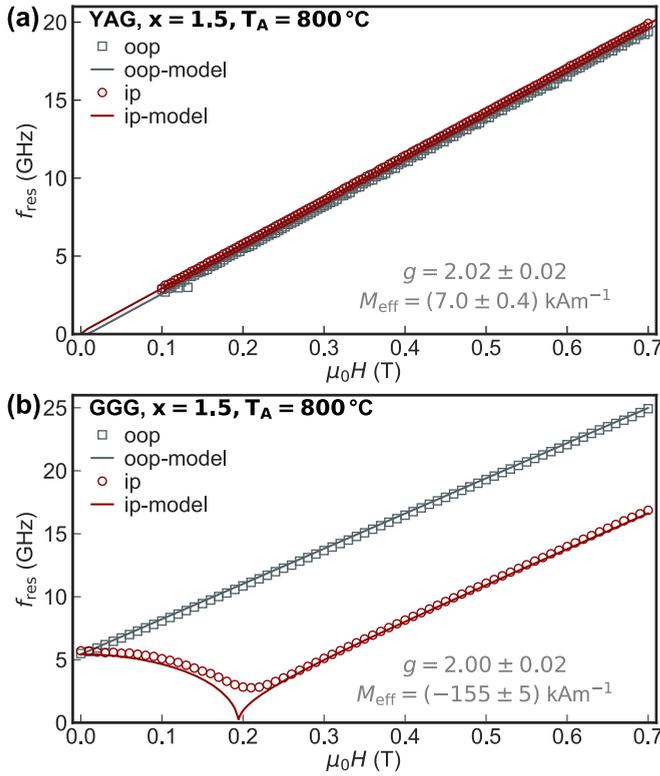$$+ \frac{1}{2}\mu_0 M_s M_{eff} cos^2\theta_M, \tag{1}$$

FIG. 7. FMR resonance f_{res} as a function of the applied magnetic field H at a temperature of 200 K for a YAlIG sample grown on YAG (a) and one sample grown on GGG (b). The modeled curve is based on the approach by Baselgia et al. [56] and the total free energy density described in Eq. (1). The corresponding M_{eff} and g are displayed in the plot.

where θ_M, ϕ_M and θ_H, ϕ_H denote the polar and azimuthal angles of the magnetization and the magnetic field, respectively. The first term in Eq. (1) describes the Zeeman energy and the second term the effective demagnetization energy. The effective magnetization $M_{\text{eff}} = M_{\text{s}} - H_{\text{u}}$ in this model includes the shape anisotropy field (equal to M_{s}) and a perpendicular uniaxial anisotropy field H_{u}.

Figures 7(a) and 7(b) show that the modeled f_{res} values are in good agreement with the experimental data. For both substrates, we extract a g factor of approximately two, which is expected for YAlIG as the magnetic moment mostly originates of electron spins. On the YAG substrate, $M_{\text{eff}} = 7.0$ kA/m which is smaller than the saturation magnetization M_{s}. We can therefore conclude that the shape anisotropy is partially compensated by a perpendicular anisotropy. This is comparable to the result of the SQUID VSM measurement, although measured at a different temperature. On the GGG substrate, M_{eff} is negative, indicating that the perpendicular magnetic anisotropy is the dominant magnetic anisotropy. Thus, it is possible to grow YAlIG on GGG as a PMA (perpendicular magnetic anisotropy) material. This large perpendicular magnetic anisotropy, in particular compared to the sample grown on YAG, is caused by a magnetoelastic anisotropy. As discussed in the XRD analysis, the YAlIG thin films grown on

GGG are epitaxially strained so that the film is under tensile strain in the film plane. In this case, previous reports also suggest a strong perpendicular magnetoelastic contribution and the possibility of PMA in rare earth garnet thin films [57–59]. We would anticipate a similar correlation for our YAlIG thin films grown on GGG.

The dynamic properties of a YAlIG thin film are evaluated based on the extracted resonance linewidth Δf. At $f_{\text{res}} = 10$ GHz, the frequency linewidth is $\Delta f = 200$ MHz for a YAlIG thin film grown on GGG, which corresponds to a magnetic field linewidth of $\Delta B = 7.1$ mT ($\Delta B = \frac{2\pi\hbar}{g\mu_B}\Delta f$). This value is within the range reported for strained rare earth garnet thin films ($\Delta B = 0.3 - 7.5$ mT) [57–60] and close to the range reported for sputtered YIG thin films ($\Delta B = 0.35 - 7$ mT) [36,57,61,62]. The Gilbert damping α is determined by evaluating the frequency dependence of the extracted resonance linewidths (not shown). In our YAlIG thin films, α is of the order of 10^{-3}, which is comparable to other sputtered garnet thin films [59,60,62], but still higher than the best values reported for highest quality YIG thin films [19].

IV. CONCLUSION

We report the successful growth of ferrimagnetic $Y_3Fe_{5-x}Al_xO_{12}$ films via RF sputtering for substitution levels of $x = 1.5, 1.75, 2$ on single crystalline YAG (111) and GGG (111) substrates. A post-annealing step in reduced oxygen atmosphere is necessary for the crystallization of YAlIG. On YAG substrates with a higher lattice mismatch, relaxed YAlIG(111) films are obtained with a higher degree of defects. The lower lattice mismatch with the GGG substrates results in the growth of fully strained perpendicular compressed YAlIG(111) layers of higher crystalline quality as compared to the samples on YAG. SQUID VSM reveals that the Curie temperature of the sputtered YAlIG thin films on YAG can be controlled by the Al^{3+} substitution level. We achieve T_{c} values down to 102 K, which is well below room temperature. We also show low coercivity comparable to other sputtered YIG thin films. Broadband-FMR measurements evidence a dominant perpendicular magnetic anisotropy in the YAlIG thin film grown on GGG caused by the epitaxial strain, whereas no such effect can be observed in the thin films grown on YAG. We also find that the FMR resonance linewidth and Gilbert damping are similar to other rare earth garnet thin films. However, the chemical composition of the YAlIG films, measured via RBS, is not equal to the nominal substitution level of the sputtering targets. This effect has to be considered for a quantitative control of the chemical composition and hence the magnetic properties of Al-substituted YIG.

[1] M. Weiler, M. Althammer, F. D. Czeschka, H. Huebl, M. S. Wagner, M. Opel, I.-M. Imort, G. Reiss, A. Thomas, R. Gross, and S. T. B. Goennenwein, Local Charge and Spin Currents in Magnetothermal Landscapes, Phys. Rev. Lett. **108**, 106602 (2012).

[2] H. Nakayama, M. Althammer, Y.-T. Chen, K. Uchida, Y. Kajiwara, D. Kikuchi, T. Ohtani, S. Geprägs, M. Opel, S. Takahashi, R. Gross, G. E. W. Bauer, S. T. B. Goennenwein, and E. Saitoh, Spin Hall Magnetoresistance Induced by a Nonequilibrium Proximity Effect, Phys. Rev. Lett. **110**, 206601 (2013).

[3] M. Althammer, S. Meyer, H. Nakayama, M. Schreier, S. Altmannshofer, M. Weiler, H. Huebl, S. Geprägs, M. Opel, R. Gross, D. Meier, C. Klewe, T. Kuschel, J.-M. Schmalhorst, G. Reiss, L. Shen, A. Gupta, Y.-T. Chen, G. E. W. Bauer, E. Saitoh, and *et al.*, Quantitative study of the spin Hall magnetoresistance in ferromagnetic insulator/normal metal hybrids, Phys. Rev. B **87**, 224401 (2013).

[4] L. J. Cornelissen, J. Liu, R. A. Duine, J. B. Youssef, and B. J. van Wees, Long-distance transport of magnon spin information in a magnetic insulator at room temperature, Nat. Phys. **11**, 1022 (2015).

[5] A. A. Serga, A. V. Chumak, and B. Hillebrands, YIG magnonics, J. Phys. D **43**, 264002 (2010).

[6] A. V. Chumak, V. Vasyuchka, A. Serga, and B. Hillebrands, Magnon spintronics, Nat. Phys. **11**, 453 (2015).

[7] S. T. B. Goennenwein, R. Schlitz, M. Pernpeintner, K. Ganzhorn, M. Althammer, R. Gross, and H. Huebl, Non-local magnetoresistance in YIG/Pt nanostructures, Appl. Phys. Lett. **107**, 172405 (2015).

[8] S. Meyer, Y.-T. Chen, S. Wimmer, M. Althammer, T. Wimmer, R. Schlitz, S. Geprägs, H. Huebl, D. Ködderitzsch, H. Ebert, G. E. W. Bauer, R. Gross, and S. T. B. Goennenwein, Observation of the spin nernst effect, Nat. Mater. **16**, 977 (2017).

[9] K. Ganzhorn, S. Klingler, T. Wimmer, S. Geprägs, R. Gross, H. Huebl, and S. T. B. Goennenwein, Magnon-based logic in a multi-terminal YIG/Pt nanostructure, Appl. Phys. Lett. **109**, 022405 (2016).

[10] M. Lammel, R. Schlitz, K. Geishendorf, D. Makarov, T. Kosub, S. Fabretti, H. Reichlova, R. Huebner, K. Nielsch, A. Thomas, and S. T. B. Goennenwein, Spin Hall magnetoresistance in heterostructures consisting of noncrystalline paramagnetic YIG and Pt, Appl. Phys. Lett. **114**, 252402 (2019).

[11] K. Oyanagi, S. Takahashi, L. J. Cornelissen, S. Shan, Juanand Daimon, T. Kikkawa, G. E. W. Bauer, B. J. van Wees, and E. Saitoh, Spin transport in insulators without exchange stiffness, Nat. Commun. **10**, 4740 (2019).

[12] K. Oyanagi, J. M. Gomez-Perez, X.-P. Zhang, T. Kikkawa, Y. Chen, E. Sagasta, A. Chuvilin, L. E. Hueso, V. N. Golovach, F. S. Bergeret, F. Casanova, and E. Saitoh, Paramagnetic spin Hall magnetoresistance, Phys. Rev. B **104**, 134428 (2021).

[13] R. Schlitz, S. Granovsky, D. Pohl, A. Thomas, B. Rellinghaus, and S. T. B. Goennenwein, Nonlocal magnon-based transport in yttrium-iron-garnet–platinum heterostructures at high temperatures, Phys. Rev. B **103**, 214434 (2021).

[14] A. Aqeel, N. Vlietstra, J. A. Heuver, G. E. W. Bauer, B. Noheda, B. J. van Wees, and T. T. M. Palstra, Spin-Hall magnetoresistance and spin seebeck effect in spin-spiral and paramagnetic phases of multiferroic CoCr$_2$O$_4$ films, Phys. Rev. B **92**, 224410 (2015).

[15] S. Martín-Rio, C. Frontera, J. M. Gã³mez-Pérez, M. X. Aguilar-Pujol, S. Catalano, J. Gã¡zquez, F. Casanova, L. Balcells, A. Pomar, and B. Martinez, Interfacial magnetic features of La$_2$CoMnO$_6$/Pt bilayers studied by using spin Hall magnetoresistance, Advanced Materials Interfaces **9**, 2201171 (2022).

[16] K.-i. Uchida, Z. Qiu, T. Kikkawa, R. Iguchi, and E. Saitoh, Spin Hall magnetoresistance at high temperatures, Appl. Phys. Lett. **106**, 052405 (2015).

[17] M. C. Onbasli, A. Kehlberger, D. H. Kim, G. Jakob, M. Kläui, A. V. Chumak, B. Hillebrands, and C. A. Ross, Pulsed laser deposition of epitaxial yttrium iron garnet films with low gilbert damping and bulklike magnetization, APL Mater. **2**, 106102 (2014).

[18] G. Schmidt, C. Hauser, P. Trempler, M. Paleschke, and E. T. Papaioannou, Ultra thin films of yttrium iron garnet with very low damping: A review, physica status solidi (b) **257**, 1900644 (2020).

[19] C. Hauser, T. Richter, N. Homonnay, C. Eisenschmidt, M. Qaid, H. Deniz, D. Hesse, M. Sawicki, S. G. Ebbinghaus, and G. Schmidt, Yttrium iron garnet thin films with very low damping obtained by recrystallization of amorphous material, Sci. Rep. **6**, 20827 (2016).

[20] C. Dubs, O. Surzhenko, R. Thomas, J. Osten, T. Schneider, K. Lenz, J. Grenzer, R. Hübner, and E. Wendler, Low damping and microstructural perfection of sub-40nm-thin yttrium iron garnet films grown by liquid phase epitaxy, Phys. Rev. Mater. **4**, 024416 (2020).

[21] Y. Krockenberger, H. Matsui, T. Hasegawa, M. Kawasaki, and Y. Tokura, Solid phase epitaxy of ferrimagnetic Y$_3$Fe$_5$O$_{12}$ garnet thin films, Appl. Phys. Lett. **93**, 092505 (2008).

[22] E. E. Anderson, Molecular field model and the magnetization of YIG, Phys. Rev. **134**, A1581 (1964).

[23] N. Thiery, V. V. Naletov, L. Vila, A. Marty, A. Brenac, J.-F. Jacquot, G. de Loubens, M. Viret, A. Anane, V. Cros, J. Ben Youssef, N. Beaulieu, V. E. Demidov, B. Divinskiy, S. O. Demokritov, and O. Klein, Electrical properties of epitaxial yttrium iron garnet ultrathin films at high temperatures, Phys. Rev. B **97**, 064422 (2018).

[24] G. R. Harrison and L. R. Hodges Jr., Microwave properties of polycrystalline hybrid garnets, J. Am. Ceram. Soc. **44**, 214 (1961).

[25] S. Geller, H. J. Williams, G. P. Espinosa, and R. C. Sherwood, Importance of intrasublattice magnetic interactions and of substitutional ion type in the behavior of substituted yttrium iron garnets, Bell Syst. Tech. J. **43**, 565 (1964).

[26] G. F. Dionne, Molecular field coefficients of substituted yttrium iron garnets, J. Appl. Phys. **41**, 4874 (1970).

[27] P. Röschmann and P. Hansen, Molecular field coefficients and cation distribution of substituted yttrium iron garnets, J. Appl. Phys. **52**, 6257 (1981).

[28] F. Grasset, S. Mornet, A. Demourgues, J. Portier, J. Bonnet, A. Vekris, and E. Duguet, Synthesis, magnetic properties, surface modification and cytotoxicity evaluation of Y$_3$Fe$_{5-x}$Al$_x$O$_{12}$($0 \leqslant x \leqslant 2$) garnet submicron particles for biomedical applications, J. Magn. Magn. Mater. **234**, 409 (2001).

[29] B. Ravi, X. Guo, Q. Yan, R. Gambino, S. Sampath, and J. Parise, Phase evolution and magnetic properties of al substituted

yttrium iron garnet nanopowders and plasma-sprayed coatings, Surf. Coat. Technol. **201**, 7597 (2007).

[30] Z. Azadi Motlagh, M. Mozaffari, and J. Amighian, Preparation of nano-sized Al-substituted yttrium iron garnets by the mechanochemical method and investigation of their magnetic properties, J. Magn. Magn. Mater. **321**, 1980 (2009).

[31] Y. Chen, K. Wu, Y. Yao, C. Peng, K. You, and W. Tse, The influence of Fe concentration on $Y_3Al_{5-x}Fe_xO_{12}$ garnets, Microelectron. Eng. **81**, 329 (2005).

[32] G. F. Dionne, Determination of magnetic anisotropy and porosity from the approach to saturation of polycrystalline ferrites, J. Appl. Phys. **40**, 1839 (1969).

[33] X. Liang, G. Shi, L. Deng, F. Huang, J. Qin, T. Tang, C. Wang, B. Peng, C. Song, and L. Bi, Magnetic Proximity Effect and Anomalous Hall Effect in $Pt/Y_3Fe_{5-x}Al_xO_{12}$ Heterostructures, Phys. Rev. Appl. **10**, 024051 (2018).

[34] J. Ding, T. Liu, H. Chang, and M. Wu, Sputtering growth of low-damping yttrium-iron-garnet thin films, IEEE Magn. Lett. **11**, 1 (2020).

[35] M. Lammel, D. Scheffler, D. Pohl, P. Swekis, S. Reitzig, S. Piontek, H. Reichlova, R. Schlitz, K. Geishendorf, L. Siegl *et al.*, Atomic layer deposition of yttrium iron garnet thin films, Phys. Rev. Mater. **6**, 044411 (2022).

[36] H. Chang, P. Li, W. Zhang, T. Liu, A. Hoffmann, L. Deng, and M. Wu, Nanometer-thick yttrium iron garnet films with extremely low damping, IEEE Magn. Lett. **5**, 1 (2014).

[37] M. Mayer, SIMNRA user's guide, Report IPP 9/113, Max-Planck-Institut für Plasmaphysik (1997).

[38] H. Maier-Flaig, Magnetic resonance of ferrimagnetic insulators, Ph.D. thesis, Technische Universität München, 2018.

[39] M. A. Gilleo and S. Geller, Magnetic and crystallographic properties of substituted yttrium-iron garnet, $3Y_2O_3 \cdot xM_2O_3 \cdot (5-x) \cdot Fe_2O_3$, Phys. Rev. **110**, 73 (1958).

[40] M. A. Musa, R. S. Azis, N. H. Osman, J. Hassan, and T. Zangina, Structural and magnetic properties of yttrium iron garnet (YIG) and yttrium aluminum iron garnet (YAlG) nanoferrite via sol-gel synthesis, Results in Physics **7**, 1135 (2017).

[41] D. Rodic, M. Mitric, R. Tellgren, and H. Rundlof, The cation distribution and magnetic structure of $Y_3Fe_{(5-x)}Al_xO_{12}$, J. Magn. Magn. Mater. **232**, 1 (2001).

[42] A. R. Bhalekar and L. N. Singh, Structural and magnetic studies of aluminum substituted YIG nanoparticles prepared by a sol-gel route, Braz. J. Phys. **49**, 636 (2019).

[43] R. Gross and A. Marx, *Festkörperphysik* (De Gruyter, Berlin, Boston, 2018).

[44] P. John, P. Vennéguès, H. Rotella, C. Deparis, C. Lichtensteiger, and J. Zuniga-Perez, Microstructure of epitaxial Mg_3N_2 thin films grown by MBE, J. Appl. Phys. **129**, 095303 (2021).

[45] M. Becht, F. Wang, J. Wen, and T. Morishita, Evolution of the microstructure of oxide thin films, J. Cryst. Growth **170**, 799 (1997).

[46] S. Webster, R. Kumaran, S. Penson, and T. Tiedje, Structural analysis of thin epitaxial Y_2O_3 films on sapphire, J. Vac. Sci. Technol. B **28**, C3A20 (2010).

[47] O. Durand, A. Letoublon, D. Rogers, and F. Hosseini Teherani, Interpretation of the two-components observed in high

resolution x-ray diffraction ω scan peaks for mosaic zno thin films grown on c-sapphire substrates using pulsed laser deposition, Thin Solid Films **519**, 6369 (2011).

[48] V. M. Kaganer, O. Brandt, H. Riechert, and K. K. Sabelfeld, x-ray diffraction of epitaxial films with arbitrarily correlated dislocations: Monte Carlo calculation and experiment, Phys. Rev. B **80**, 033306 (2009).

[49] S. Geller, G. P. Espinosa, and P. B. Crandall, Thermal expansion of yttrium and gadolinium iron, gallium and aluminum garnets, J. Appl. Crystallogr. **2**, 86 (1969).

[50] C. Wu, C.-C. Tseng, K. Lin, C. Cheng, S. Yeh, Y. Fanchiang, M. Hong, and J. Kwo, High-quality single-crystal thulium iron garnet films with perpendicular magnetic anisotropy by off-axis sputtering, AIP Adv. **8**, 055904 (2018).

[51] M.-B. Park and N.-H. Cho, Structural and magnetic characteristics of yttrium iron garnet (YIG, Ce : YIG) films prepared by RF magnetron sputter techniques, J. Magn. Magn. Mater. **231**, 253 (2001).

[52] M. Chern, W. Lee, and D. Liou, Curie temperatures of $Y_3Fe_5O_{12}/Gd_3Fe_5O_{12}$ superlattices, J. Magn. Magn. Mater. **170**, L243 (1997).

[53] T. Takeuchi, N. Ohta, and Y. Sugita, Curie temperatures and anisotropy fields in very thin garnet films, J. Magn. Magn. Mater. **31-34**, 925 (1983).

[54] G. Vértesy and I. Tomáš, Survey of the dependence on temperature of the coercivity of garnet films, J. Appl. Phys. **77**, 6426 (1995).

[55] A. Mitra, Structural and magnetic properties of yig thin films and interfacial origin of magnetisation suppression, Ph.D. thesis, University of Leeds, 2017.

[56] L. Baselgia, M. Warden, F. Waldner, S. L. Hutton, J. E. Drumheller, Y. Q. He, P. E. Wigen, and M. Maryško, Derivation of the resonance frequency from the free energy of ferromagnets, Phys. Rev. B **38**, 2237 (1988).

[57] J. Ding, C. Liu, Y. Zhang, U. Erugu, Z. Quan, R. Yu, E. McCollum, S. Mo, S. Yang, H. Ding *et al.*, Nanometer-Thick Yttrium Iron Garnet Films with Perpendicular Anisotropy and Low Damping, Phys. Rev. Appl. **14**, 014017 (2020).

[58] L. Soumah, N. Beaulieu, L. Qassym, C. Carrétéro, E. Jacquet, R. Lebourgeois, J. Ben Youssef, P. Bortolotti, V. Cros, and A. Anane, Ultra-low damping insulating magnetic thin films get perpendicular, Nat. Commun. **9**, 3355 (2018).

[59] O. Ciubotariu, A. Semisalova, K. Lenz, and M. Albrecht, Strain-induced perpendicular magnetic anisotropy and gilbert damping of $Tm_3Fe_5O_{12}$ thin films, Sci. Rep. **9**, 17474 (2019).

[60] X. Liu, Q. Yang, D. Zhang, Y. Wu, and H. Zhang, Magnetic properties of bismuth substituted yttrium iron garnet film with perpendicular magnetic anisotropy, AIP Adv. **9**, 115001 (2019).

[61] S. Yamamoto, H. Kuniki, H. Kurisu, M. Matsuura, and P. Jang, Post-annealing effect of YIG ferrite thin-films epitaxially grown by reactive sputtering, physica status solidi (a) **201**, 1810 (2004).

[62] B. Bhoi, N. Venkataramani, R. P. R. C. Aiyar, S. Prasad, and M. Kostylev, Effect of annealing on the structural and FMR properties of epitaxial YIG thin films grown by RF magnetron sputtering, IEEE Trans. Magn. **54**, 1 (2018).